



CH and NO planar laser-induced fluorescence and Rayleigh-scattering in turbulent flames using a multimode optical parametric oscillator

JOSEPH D. MILLER,¹  JOHANNES W. TRÖGER,^{2,3} SASCHA R. ENGEL,^{2,4} THOMAS SEEGER,^{2,3} ALFRED LEIPERTZ,^{2,4} AND TERRENCE R. MEYER^{2,5,*} 

¹Air Force Research Laboratory, Wright-Patterson Air Force Base, Dayton, Ohio 45433, USA

²Erlangen Graduate School in Advanced Optical Technologies (SAOT), 91052 Erlangen, Germany

³Lehrstuhl für Technische Thermodynamik, Universität Siegen, 57076 Siegen, Germany

⁴Lehrstuhl für Technische Thermodynamik, Friedrich-Alexander-Universität Erlangen-Nürnberg, 91052 Erlangen, Germany

⁵School of Mechanical Engineering, Purdue University, West Lafayette, Indiana 47907, USA

*Corresponding author: trmeyer@purdue.edu

Received 28 September 2020; revised 22 November 2020; accepted 26 November 2020; posted 1 December 2020 (Doc. ID 406237); published 22 December 2020

An optical parametric oscillator (OPO) is developed and characterized for the simultaneous generation of ultraviolet (UV) and near-UV nanosecond laser pulses for the single-shot Rayleigh scattering and planar laser-induced-fluorescence (PLIF) imaging of methylidyne (CH) and nitric oxide (NO) in turbulent flames. The OPO is pumped by a multichannel, 8-pulse Nd:YAG laser cluster that produces up to 225 mJ/pulse at 355 nm with pulse spacing of 100 μ s. The pulsed OPO has a conversion efficiency of 9.6% to the signal wavelength of \sim 430 nm when pumped by the multimode laser. Second harmonic conversion of the signal, with 3.8% efficiency, is used for the electronic excitation of the A-X (1,0) band of NO at \sim 215 nm, while the residual signal at 430 nm is used for direct excitation of the A-X (0,0) band of the CH radical and elastic Rayleigh scattering. The section of the OPO signal wavelength for simultaneous CH and NO PLIF imaging is performed with consideration of the pulse energy, interference from the reactant and product species, and the fluorescence signal intensity. The excitation wavelengths of 430.7 nm and 215.35 nm are studied in a laminar, premixed CH₄-H₂-NH₃-air flame. Single-shot CH and NO PLIF and Rayleigh scatter imaging is demonstrated in a turbulent CH₄-H₂-NH₃ diffusion flame using a high-speed intensified CMOS camera. Analysis of the complementary Rayleigh scattering and CH and NO PLIF enables identification and quantification of the high-temperature flame layers, the combustion product zones, and the fuel-jet core. Considerations for extension to simultaneous, 10-kHz-rate acquisition are discussed. © 2020 Optical Society of America

<https://doi.org/10.1364/AO.406237>

1. INTRODUCTION

Turbulent combustion processes are fundamental to many engineering applications, including aerospace propulsion systems, home heating furnaces, and industrial boilers [1]. In these reacting flows, the spatial and temporal evolution of flame species impact combustion stability and efficiency and are highly dependent on complex fluid-flame interactions. These spatiotemporal interactions, along with the fuel compositional effects, can lead to elevated production of harmful pollutant emissions including carbon monoxide (CO), formaldehyde (CH₂O), polycyclic aromatic hydrocarbons (PAH), nitric oxides (NO_x), and soot [2]. Nitric oxide (NO) is of particular importance in the combustion of biomass-derived fuels where fuel-born nitrogen, trace amounts (1–3%) of ammonia (NH₃),

and hydrocarbon radicals can result in NO levels nearing 3000 parts per million (ppm), well outside the established environmental limits [3,4]. Specifically, the presence of methylidyne (CH) can play a significant role in the prompt formation of NO via the Fenimore Mechanism [5]. To understand the impact of prompt NO formation in the combustion of biomass-derived fuels, Li studied CH and NO production in non-premixed, laminar combustion of syngas mixtures using planar laser-induced fluorescence (PLIF) [4]. The quantification of the NO PLIF signals enabled comparisons with established chemical mechanisms in laminar flames where the measurement rate of 10 Hz was sufficient to capture fluid-flame interactions. However, the spatiotemporal investigation of CH and NO formation in turbulent flames relevant to NH₃ and biomass-derived fuels

requires PLIF imaging at rates in excess of 1 kHz to capture the relevant fluid time scales [3]. Until recently, the absence of high-energy, high-repetition-rate sources and detectors have severely limited the application of PLIF imaging of minor species (i.e., NO, CH) for capturing transient phenomena in the turbulent combusting flows.

Over the past two decades, the development of high-energy, high-repetition-rate laser systems has enabled the extension of many fundamental spectroscopic techniques (PLIF, Rayleigh scattering, Raman scattering) to kHz and even MHz repetition rates [6]. These high-speed systems can be grouped into three broad categories: continuous diode-pumped solid-state (DPSS) lasers, clustered multichannel laser systems, and burst-mode lasers. Wavelength conversion and tuning with kHz-rate DPSS lasers is typically limited to high-speed dye lasers, due to low visible and UV pulse energies. Even so, numerous combustion diagnostics have been employed, including OH PLIF at rates up to 50 kHz [7,8], velocity and formaldehyde imaging [9,10], and CH PLIF at 10 kHz using C-X excitation near 315 nm, which can also be used for OH PLIF in a so-called two-color scheme [11]. Lee *et al.* targeted NO production in flames and flows in which NO/N₂ mixtures could be seeded into the flow [12].

Clustered multichannel Nd:YAG laser systems provide > 100 mJ at UV wavelengths (355 nm) and rates above 10 kHz, but these are limited to 4 to 8 pulses before further scaling becomes impractical. These systems have sufficient pulse energy for pumping solid-state optical parametric oscillators (OPO), which do not suffer from saturation and limitations in repetition rate common to dye lasers. Previous work has focused on OH and CH PLIF at 10 kHz [13–15]. Burst-mode Nd:YAG lasers can achieve similarly high energies with longer duration pulse trains using flashlamp-pumped (bursts up to 10 ms) [16] or diode-pumped amplifiers (bursts up to 100 ms) [17,18]. Burst-mode systems have been used to generate 1–10 mJ/pulse at UV wavelengths using OPO devices at 10 kHz or higher. The combination of a high pulse repetition rate and an extended burst duration yields sequences with 100–10,000 individual pulses, sufficient for statistical analysis of transient events [19]. This architecture has been used for kHz–MHz PLIF of NO [20], OH [21], CH [22], and CH₂O [17,23].

Nearly all of these high-speed systems rely on additional wavelength-generation schemes to produce UV laser light for laser-induced fluorescence imaging. OPO devices have found great use with clustered and burst-mode systems, where pulse energy is high and repetition rates can reach 100 kHz–MHz rates. Under these conditions, dye lasers are limited by saturation of the dye and are typically not efficient, although recent work has demonstrated the potential of burst-mode dye-laser systems for kHz-rate PLIF imaging [24]. The burst-mode pumping of a dye laser at 7.5 kHz over 75 pulses was demonstrated with an input of up to 100 mJ per pulse at 532 nm, producing 15 mJ per pulse at 566 nm and 2.2 mJ per pulse at 283 nm after second harmonic generation. However, at a pump rate of 20 kHz, a pump energy of 27 mJ at 532 nm led to dye saturation and limited the 566 nm pulse energy to 4 mJ. An additional advantage of OPO devices is narrow-bandwidth output (<0.01 cm⁻¹), when employing injection seeding with external cavity diode lasers. For this reason, OPO devices

have found considerable application in high-resolution spectroscopy using Q-switched 10-Hz sources in addition to the aforementioned high-repetition-rate sources.

In addition to high-speed, spatially resolved imaging, simultaneous multi-species and multi-parameter measurements (e.g., species and temperature) are needed to support modeling efforts. In flames with biomass-derived fuels, for example, important temperature-dependent chemical pathways for NO formation from fuel-bound nitrogen atoms in the presence of ammonia are of interest [3], along with the effects of CH on prompt NO formation in hydrocarbon flames. Multi-species measurements have been performed in standard flames using independent measurements under identical conditions, as well as using multiple laser systems for simultaneous measurement of up to three parameters, including velocity and species such as OH, formaldehyde or hydrocarbon fuels [9,25]. The former approach does not capture the transient physicochemical interactions of interest, while the latter requires multiple burst-mode lasers or highly specialized sources, such as a “three-legged” burst-mode laser system [26]. Alternatively, tunable devices that provide laser radiation at multiple wavelengths for electronic excitation of multiple combustion species and parameters such as temperature using a single high-speed laser pump source can be devised.

In this paper, we describe and characterize a single OPO with external second harmonic generation (SHG) for simultaneously tunable laser radiation at 430 nm for CH PLIF and Rayleigh scattering and 215 nm for NO PLIF using a single, multimode, Nd:YAG laser cluster as a pump source. For simplicity, we will refer to the scheme as CH–NO PLIF. While this pump-laser architecture has been demonstrated previously for CH PLIF at rates of 10 kHz by the co-authors [13], this work focuses on the characterization of the dual-wavelength OPO source and the potential for single-shot multi-parameter imaging. A particular advantage of the OPO system is the compatibility of the wavelength generation scheme with either narrow-bandwidth or multi-mode pump sources, typical of burst-mode or clustered laser systems, respectively. Additionally, the OPO architecture applied here has previously been used with burst-mode lasers at rates of 10–1000 kHz. A key challenge, however, is limited pulse energy in UV wavelengths. Hence, it is of interest if reasonably high signal levels can be achieved using high-speed intensified camera technology for measurements of various parameters of interest using CH–NO PLIF and Rayleigh scattering with a single laser source.

2. EXPERIMENTAL DETAILS

A. Optical Parametric Oscillator and Second Harmonic Generation

Adapting an OPO design described in previous publications by the authors [13,14], the current work focuses on the simultaneous generation of near-UV/UV wavelengths that are optimal for exciting CH–NO PLIF with sufficient energy to yield quantitative measurements of multiple flame parameters. Briefly, a clustered Q-switched Nd:YAG laser with pulse width of 8 ns, pulse energy as high as 225 mJ at 355 nm, and inter-pulse spacing of 100 μs was used to pump an OPO as shown in Fig. 1(a). The OPO consists of two BBO crystals

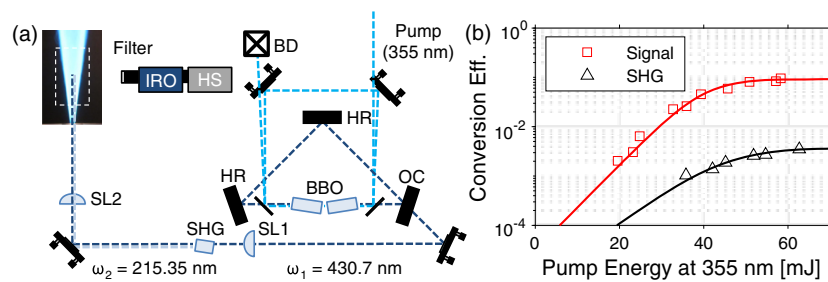


Fig. 1. (a) Optical parametric oscillator and experimental setup. Beam propagation is clockwise in the OPO ring cavity. BBO: β -barium borate crystal; HR: high reflector; OC: output coupler; BD: beam dump; SL1: 200-mm spherical lens; SHG: second harmonic generation; SL2: 500-mm spherical lens; IRO: intensifier; HS: high-speed camera. (b) Conversion efficiency to signal at 430 nm and the SHG output at 215 nm. The trend is identified using a logistics function.

($\theta_{\text{cut}} = 35^\circ$) rotated for walk-off compensation, housed in a ring cavity with a 40% output coupler. The signal output is tunable from ~ 424 – 432 nm by counter-rotation of the BBO crystals, achieving a nearly uniform spectral bandwidth of ~ 9 cm^{-1} . In this work, the OPO signal is frequency doubled using a third BBO crystal ($\theta_{\text{cut}} = 70^\circ$) located outside the OPO cavity. The SHG process produces ~ 215 -nm radiation (ω_2) with residual fundamental radiation near 430 nm (ω_1). To increase the SHG efficiency, the OPO signal beam was focused using a 200-mm spherical lens with the SHG crystal placed within 1 cm of the focal point. The UV and near-UV beams propagate collinearly and are directed into the flame using a series of right-angled, fused silica prisms with broadband UV anti-reflection coatings. The 200-mm spherical lens, used to increase the SHG efficiency, was rotated to produce a vertically elongated, divergent beam and allowed to expand after the SHG crystal. The beam was focused into a thin sheet using a 500-mm spherical lens, and the low intensity wings of the beam were blocked to produce a relatively uniform 25-mm-tall laser sheet in the flame, as shown in Fig. 1(a).

The measured conversion efficiency of the OPO and SHG processes are given in Fig. 1(b) as a function of pump energy at 355 nm. The conversion efficiency is defined as the ratio of the pulse energy at 430 nm or 215 nm to the input pulse energy at 355 nm and thus represents the total efficiency of conversion to each output wavelength. The individual energies were measured by inserting a Pellin–Broca prism into the beam path to separate the two output wavelengths. Similar to previous results [14], the single-pass OPO produces up to 4.3 mJ at 430 nm, representing a conversion efficiency of 7.3%. The spectral bandwidth of the signal was measured to be 7.6 cm^{-1} , within the range of previous non-seeded, multimode pumped OPO sources (8.2 ± 1.4 cm^{-1}) [14]. When double-passing the pump pulse, the OPO signal is increased to 5.6 mJ for a conversion efficiency of 9.6%. At this output energy, the SHG produces 225 μJ at 215 nm, with an SHG efficiency of $\sim 3.8\%$ and overall conversion efficiency of $\sim 0.35\%$ from the 355-nm pump beam. The SHG conversion efficiency is low and can be increased by focusing the beam into the crystal to increase energy density; however, the benefit is limited by damage to the crystal and the acceptance angle/bandwidth of the crystal. The pulse energies represented in Fig. 1(b) include losses from reflections off the 200-mm lens used to focus the signal beam. The multi-pass pump configuration has been used in prior work to increase the

OPO efficiency, but this reduces the signal beam quality when forming the laser sheet. As such, measurements in this work were conducted with the OPO in single-pass mode at reduced pump energy to avoid damage to the crystal coatings. For all the conditions in this paper, the pulse energies of ~ 2.5 mJ at 430 nm and ~ 200 μJ at 215 nm were measured at the flame location. These values are disproportionately lower than the measured OPO output values as a result of differences in the anti-reflective coatings of the sheet-forming optics.

B. PLIF Imaging System

CH–NO PLIF and Rayleigh scattering signals were detected using a high-speed CMOS camera (Photron, SA5) coupled to a high-speed dual-stage intensifier (LaVision, HS-IRO) [14]. A 45.5-mm F/1.8 UV lens (Sodern, Cerco 2073) was used to image the signal, along with two 8-mm extension rings for increasing spatial resolution with no pixel binning. The lens allowed greater than 10% transmission from 230 nm to 675 nm with a peak transmission of 93%. For detection of NO PLIF, a UG11 color-glass filter was used with a greater than 5% transmission from 250–395 nm and a peak transmission of $\sim 80\%$. This ensured sufficient suppression of elastic laser scattering at 215 nm and 430 nm, as well as CH fluorescence around 431 nm. For the detection of CH PLIF and Rayleigh scattering, a GG400 color-glass filter was used with a greater than 50% transmission above 400 nm and a peak transmission of $\sim 90\%$. This ensured sufficient suppression of elastic scatter at 215 nm and NO fluorescence that occurs below 395 nm. As discussed in our previous publication, this filter does not eliminate elastic scatter at 430 nm such that Rayleigh scattering is present in the images [14]. In this case, care was taken to avoid saturation of the detector and intensifier resulting from scatter off surfaces and large particles. Additionally, discrimination of the Rayleigh scattering and CH PLIF signals required the subtraction of the “off-resonant” images where Rayleigh scatter was present, but the excitation wavelength was selected to avoid CH absorption.

Typically, simultaneous PLIF imaging requires a separate camera for each species to optimize detection. In this work, only one camera/intensifier combination was used to acquire both the Rayleigh scatter and CH–NO PLIF signals in a premixed laminar flame. No spectral filtering was used for this purpose, with signals integrated from 230 to 675 nm, including NO PLIF, Rayleigh scatter at 430 nm, CH PLIF, and background

flame emission. As a result, identification of the individual structures associated with each signal required interpretation based on known flame structure and combustion chemistry. This was performed in a similar manner to other “two-color” schemes such as CH–OH PLIF [11]. While this demonstrated the feasibility of simultaneous imaging, characterization of the dual-wavelength CH–NO PLIF and Rayleigh scattering approach was performed with independent acquisition of the signals. In this case, both wavelengths were generated simultaneously and were absorbed in the flame, but either the GG400 or UG11 filter were used with the single camera/intensifier to limit fluorescence detection to Rayleigh scatter and CH PLIF or NO PLIF, respectively. This allowed optimization of the PLIF signals, separation of Rayleigh scatter and CH PLIF at 430 nm, and proper selection of the OPO signal to meet CH–NO PLIF detection requirements.

C. Laminar Premixed and Turbulent Diffusion Flames

Two types of flames were utilized in this work, with specific emphasis placed on NH_3 seeding relevant to biomass-derived fuels. Both flames were stabilized over a jet burner with a 2-mm-diameter round orifice surrounded by an axisymmetric co-flow of air. A laminar premixed CH_4 – H_2 – NH_3 –air flame with varying levels of CH_4 and NH_3 was used for characterization of the simultaneous CH–NO PLIF approach. The fuel mixture was composed of 55% H_2 by volume with a balance ranging from 45–10% NH_3 and 0–35% CH_4 , respectively. The fuel was premixed with air to an equivalence ratio of 1.4 and Reynolds number of ~ 1090 . The laminar flame is comparable to that used in our previous work (Ref. [14], Fig. 7), where the CH_4 has been partially or fully replaced with NH_3 while maintaining the same equivalence ratio. The amount of CH_4 was chosen to vary CH and NO production for characterization purposes. This flame was chosen for its well-defined flame structure and high levels of CH and NO and enabled evaluation of the PLIF and Rayleigh scattering approach.

A turbulent non-premixed diffusion flame was used to demonstrate single-shot PLIF imaging of CH and NO along with Rayleigh scattering at 430 nm. The fuel mixture was comprised of 2.2% NH_3 , 7.9% H_2 , and 89.9% CH_4 by volume with a total flow rate of 12.7 SLPM resulting in a jet Reynolds number of ~ 7570 . An air co-flow of 1.35 SLPM was provided. This flame is comparable to our previous work (Ref. [14], Fig. 11c) with 4% CH_4 replacement to achieve 2.2% NH_3 seeding, indicative of biomass derived synthetic gases [4]. Hydrogen was added to decrease the formation of polycyclic aromatic hydrocarbons (PAH) that are broadband absorbers and obscure the thin CH layer [27]. Calculations using a computational fluid dynamics with chemistry (CFDC) code known as UNICORN (UNsteady Ignition and Combustion with ReactionNs, Innovative Scientific Solutions, Inc.), indicate that NO concentrations in the NH_3 -seeded flames are ~ 1000 – 2000 ppm [4].

3. SELECTION OF EXCITATION WAVELENGTHS

For simultaneous CH and NO PLIF, an excitation wavelength must be chosen which provides sufficient CH PLIF signal near

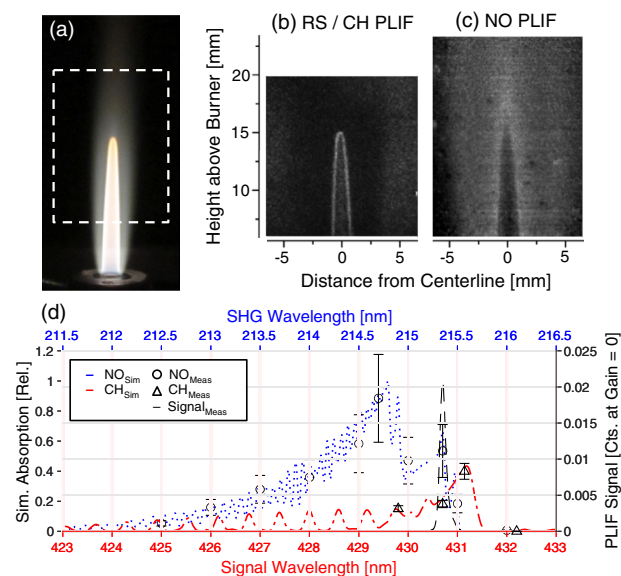


Fig. 2. (a) Visual image of laminar, premixed CH_4 – H_2 – NH_3 –air flame. The white box indicates the region of interrogation for (b) Rayleigh scattering and CH PLIF and (c) NO PLIF. Images are acquired from a single laser shot. (d) OPO signal at 430.7 nm overlaid with excitation scan over the NO (top axis) and CH (bottom axis) absorption profiles compared with LIFBASE simulations [28]. The NO absorption spectrum was modeled at 1750 K and an instrument function of 7.9 cm^{-1} . Experimental measurements (open symbols, right axis) are corrected for intensifier gain, averaged over 100 images, and bars represent the measured noise-to-signal ratios.

430 nm and, simultaneously, NO PLIF signal with excitation near 215 nm. Additionally, the resonant Rayleigh scatter from the combustion gases must be balanced with the CH PLIF signal, as both are acquired in the same image. The physics-based, empirically driven selection of the wavelength was performed using CH and NO PLIF signals and Rayleigh scattering in the laminar CH_4 – H_2 – NH_3 –air flame discussed previously and shown in Fig. 2(a). The cone-like structure of the thin flame layer is clearly visible, surrounded by a hot product region. The white dashed box represents the region interrogated with CH and NO PLIF.

A. Spectroscopic Considerations for NO and CH PLIF and Rayleigh Scattering

NO PLIF imaging has been used extensively in combustion and high-speed flow systems to understand pollutant formation, chemical kinetics, and turbulent mixing [3,5,20]. For these applications, the A–X (0,0) vibrational band at 226 nm is commonly used, as it is easily accessible using commercial off-the-shelf dye laser technology. However, in this work, the A–X (1,0) band near 215 nm was utilized, with fluorescence occurring primarily from 220–350 nm [28]. The UV lens used in this work is opaque below 230 nm, acting as a filter for elastic scatter and resonant fluorescence, while the UG11 filter acts as a band pass to eliminate Rayleigh scattering and CH PLIF at 430 nm. The NO fluorescence is integrated over the region of 250–395 nm, limited primarily by the UG11 filter and UV lens transmission.

CH PLIF imaging has been used to mark the primary reaction zone in hydrocarbon flames and study combustion stability [29,30]. In most cases, excitation of the B-X (0,0) vibrational band is used with fluorescence detection from 422–435 nm, allowing filtering of elastic scatter at the excitation wavelength [29]. Recently the C-X (0,0) transition at 315 nm has also been used because of its overlap with OH A-X (0,0) transitions [11]. As in our prior work [14], here we utilize the CH A-X (0,0) band at 430 nm for excitation with resonant detection of fluorescence. As a result, other resonant scattering processes may also be integrated along with the CH PLIF signal, including Rayleigh and Mie scattering. Proper spectral filtering can remove Rayleigh scattering from the surrounding cold air and elastic Mie scattering from particles while maintaining sufficient CH PLIF above 431 nm. However, for unconfined flames and clean gas flows Mie scattering from surfaces or particles is rare, and Rayleigh scattering can be used to identify hot product regions that are spatially distinct from the thin, high-temperature flame layers [14]. For this reason, a GG400 long-pass filter is used in the current work to suppress contributions from the NO PLIF signal, while integrating Rayleigh scattering and resonant CH fluorescence from 420–440 nm.

Rayleigh scattering from molecular species can be used to quantify the density and temperature of combustion processes if the composition is known. Significant work has focused on the measurement of differential Rayleigh scattering cross sections of combustion-relevant species as a function of temperature and scattering wavelength [31]. If the composition of a gas-phase sample is known, the relative Rayleigh cross section can be estimated as a function of scattering wavelength and number density. Assuming an ideal gas equation of state, Rayleigh scattering can then be related to the temperature of the gas sample. When coupled with recent advances in high-energy, high-repetition-rate laser sources, these measurements can enable planar temperature measurements in “canonical” turbulent diffusion flames, often with strict compositional requirements that produce uniform scattering cross sections in both the reactants and the burned products [32]. Rayleigh scattering at 430 nm benefits from increased scattering relative to 532 nm, which is commonly used in Rayleigh thermometry, while avoiding depolarization issues encountered with UV wavelengths. In addition, the quantum efficiency of the high-speed intensifier used in this work is also ~5% higher at 430 nm than at 532 nm. Hence, while the per-pulse energy at 430 nm (<5 mJ) is significantly lower than at 532 nm (~500 mJ), it is feasible to detect Rayleigh scattering as a by-product of the illumination system. However, this requires the use of an intensified camera. Here, the composition was not made to conform to uniform Rayleigh cross-sectional requirements, and the product species composition is not known at each point in space and time. As such, the differential Rayleigh cross sections of the co-flow air, fuel, and combustion products can vary by a factor of ~2 in the CH₄–H₂–NH₃ diffusion flame, and only qualitative temperature information can be extracted from the Rayleigh scattering at 430 nm.

B. OPO Signal Wavelength Selection Criteria

Because the NO and CH PLIF excitation wavelengths are derived from the same source, judicious selection of the OPO signal wavelength is required to optimize simultaneous CH–NO PLIF signal generation and, to a lesser extent, Rayleigh scattering. The selection criteria for the OPO signal wavelength can be categorized as follows: available pulse energy, interference from scattering and broadband absorbers, and the strength of the fluorescence signal. A full treatment of CH and NO PLIF, including quenching and reabsorption, and Rayleigh scattering is beyond the scope of this work. However, an empirical investigation of the relative CH and NO PLIF intensity and Rayleigh scattering is used to guide selection of the OPO signal wavelength.

First, the recorded fluorescence signal and Rayleigh scattering is directly related to the laser pulse energy per spectral element at a given wavelength. The available pulse energy is 2.5 mJ at 430 nm and 225 μJ at 215 nm. Within the relevant wavelength ranges for CH and NO PLIF, 420–440 nm and 211–216 nm, respectively, the OPO conversion efficiency and bandwidth are nearly uniform [14]. As a result, the second harmonic conversion efficiency is also uniform across the range and there is no significant advantage to a specific wavelength on the basis of pulse energy. While injection seeding of the OPO provides a significant increase in signal conversion efficiency (up to 12%) and narrows the bandwidth by a factor of 2 (~4.4 cm⁻¹) [14], a suitable tunable seed laser was not available over the wavelength range required for this work.

Second, interference in the fluorescence image can originate from elastic scattering of the particles (Mie scattering), while fluorescence from fuel (NH₃) and products (PAH) can yield interfering fluorescence signals within the same wavelength range. The former produce spatially localized “hot spots” in the image, which can be difficult to remove in post-processing and can, potentially, damage sensitive imaging systems. The latter results in spatially broad, background signals that can interfere with interpretation of the PLIF signal. Elastic scattering at 215 nm was blocked by the UV lens which exhibits 0% transmission below 220 nm. At 430 nm, both Rayleigh scattering and Mie scattering are transmitted by the optical system. Care was taken to eliminate particulates in the fuel jet and co-flow air, to minimize scattering from the burner surface, and to minimize secondary reflections. Specifically, filtered compressed gases were used for all fuels and air co-flow, data was collected ~10 mm above the burner surface to minimize scattering, and non-combusting flow background images were subtracted from all PLIF images. Only Rayleigh scattering from the 430-nm wavelength is visible in the CH PLIF images (outside the hot product region and within the cooler core of the flame) and can be spatially discriminated from the thin CH PLIF layers, as shown in Fig. 2(b). In contrast, the NO PLIF signal broadly fills the product region of the flame as shown in Fig. 2(c). Figure 2(b) was collected with the 215-nm signal blocked, while Fig. 2(c) captured Rayleigh scattering (RS), CH PLIF, and NO PLIF. The NO PLIF signal is extracted by subtracting the RS/CH PLIF image. Variations in the PLIF signal resulting from the non-uniform beam profile were corrected using Rayleigh scattering from the cold ambient air in the 430-nm image. Because the

430-nm and 215-nm sheet profiles were qualitatively similar, the 430-nm beam profile was applied to both sets of images as a first order correction.

In addition to NO, NH₃ exhibits significant absorption in the UV region [33]. Because the fuel consisted of up to 45% NH₃ by volume, a wavelength scan of the NO absorption profile was obtained in the products of the laminar flame with fuel comprised of only H₂ and NH₃. This case was chosen as the NH₃ volume fraction was at its highest, and potential interference would be maximized. The laser wavelength was scanned by angle tuning the BBO crystals in the OPO, and the PLIF signal was recorded as a function of excitation wavelength. Only the 215-nm beam was transmitted to the flame for this measurement (using a Pellin Broca prism for separation). The spectrally integrated PLIF signal was averaged over a nearly uniform region ~2.5 mm outside the jet core, corrected for the intensifier gain, and normalized by the average pulse energy. For comparison, the “gain free” PLIF signal, $I_{\text{Norm},0}$ (counts/J) was calculated as

$$I_{\text{Norm},0} = \frac{I_{\text{Meas}}}{E_p \exp(bG)},$$

where I_{Meas} is the measured average PLIF counts, E_p is the pulse energy in J, b is an intensifier constant, and G is the intensifier gain. For NO PLIF, the intensifier constant was measured as $b = 0.161 \text{ Gain}^{-1}$. The gain-free PLIF signal allows direct comparison of CH and NO signals corrected for differences in the intensifier response and pulse energy between 430 nm and 215 nm. The gain-free NO PLIF signal is given as a function of wavelength in Fig. 2(d), along with a simulated NO absorption spectrum. For empirical comparison with the CH PLIF signal, the integrated NO PLIF signal is given as the product of the gain-free, normalized PLIF signal and the 215-nm pulse energy, $I_{\text{Norm},0} \times E_p$, in counts. The error bars in the experimental data represent the noise-to-signal ratio of NO PLIF signal measured in the laminar flame. The measured NO PLIF data agrees well with the simulated NO absorption spectrum from LIFBASE [28]. In general, integrated fluorescence arising from excitation at a specific wavelength is linearly related to the molecular absorption at that wavelength. This implies that the PLIF signal recorded with a 215-nm excitation originates from NO molecules and not fuel-bound NH₃. Additionally, no PLIF signal is observed in the jet core in Fig. 2(c), further confirming the signal does not originate from NH₃.

Third, the strength of the fluorescence signal between NO and CH must be considered when choosing an OPO signal wavelength. CH PLIF signal was acquired in the thin flame layer and presented as “gain-free” counts in Fig. 2(d), following the same procedure as that performed for NO PLIF. The simulated absorption profile of CH is given as a function of wavelength in Fig. 2(d). The CH profile is simulated using LIFBASE at 2000 K, corresponding roughly to the expected flame temperature, while the NO absorption was simulated at 1750 K, corresponding roughly to the expected product temperature [4]. The simulated absorption is normalized to the peak intensity in the relevant wavelength range and scaled to match the measured NO or CH PLIF signal. This is done to aid in comparison of the simulated absorption spectra and integrated PLIF signal. The signal wavelength region from 429 nm to 431.5 nm is

particularly interesting due to the significant overlap of the CH and frequency-doubled NO absorption profiles. Although not shown in the Fig. 2(d), NH₃ and CH₂O exhibit no significant absorption features in this region as discussed previously [33,34].

For the purposes of this work, the spatially and spectrally integrated PLIF signal from CH and NO was used to empirically compare the excitation and detection system performance and provide informed selection of the OPO signal wavelength. To compare the system performance as a function of the OPO signal wavelength, both CH and NO integrated PLIF signals were acquired as a function of excitation wavelength. For NO, the excitation wavelength was scanned in steps of 0.5 nm from 212.5 nm to 216 nm along with 214.7 nm. The PLIF signal was measured in the products region and integrated from 220 nm to 395 nm based on the transmission of the UV lens and UG11 color-glass filter. The “gain-free” integrated signal was scaled by the pulse energy at ~215 nm, corrected for the intensifier response ($b_{\text{NO}} = 0.161 \text{ Gain}^{-1}$), and shown with error bars representing the noise-to-signal ratio in Fig. 2(d). For CH, excitation wavelengths of 429.6 nm, 430.7 nm, 431.14 nm, and 432.2 nm were investigated. PLIF was measured along the thin flame layer and integrated from 430 nm to 500 nm based on the transmission of the UV lens and GG400 color-glass filter. Rayleigh scattering did not contribute significantly to the signal in the CH layers (<20%), confirmed by comparison to off-resonant images at 432.2 nm. The “gain-free” integrated signal was scaled by the pulse energy at ~430 nm, corrected for the intensifier response ($b_{\text{CH}} = 0.184 \text{ Gain}^{-1}$) [14], and shown with error bars representing the noise-to-signal ratio in Fig. 2(d).

C. OPO Signal Wavelength Evaluation and Selection

An appropriate OPO signal wavelength is selected by comparing the relative “gain-free” PLIF intensity, UV and near-UV pulse energy, and interferences as a function of wavelength as shown in Fig. 2(d). Generally, the “gain-free” NO PLIF signal shows higher intensity than the CH PLIF signal, even though the pulse energy available at 430 nm is ~9 × larger than at 215 nm. Notably, for OPO signal from 429.5 nm to 431.5 nm the corresponding NO PLIF signal decreases with increasing wavelength, while the CH PLIF signal increases with increasing wavelength. This range is particularly important as it is near the absorption peak for each species. By considering the sum of the CH and NO absorption profiles, scaled according to achievable PLIF intensity with the current system, three potential OPO signal wavelengths are identified: 429.8 nm, 430.7 nm, and 430.9 nm. In addition to the sum of CH and NO PLIF, which is indicative of the total signal intensity, two other metrics can be considered for evaluation of the OPO signal wavelength. First, the NO-to-CH ratio indicates the balance of the NO and CH signals. Second, the uniformity of the sum of the NO and CH signals (NO + CH) as a function of excitation wavelength indicates insensitivity of the total PLIF signal to changes in the excitation wavelength, which eases the precision required for efficient excitation. The evaluated metrics are given for all three wavelengths in Table 1. At 430.7 nm, the total signal level is only 10% lower than the peak at 429.8 nm, however, the ratio of NO/CH “gain-free” PLIF intensity is 50% that at 429.8 nm.

Table 1. Comparison of Optimal OPO Signal Wavelengths

OPO Signal (nm)	NO + CH (Norm.)	NO/CH (Rel.)	Uniform Band (nm)
429.8	1	6.21	0.11
430.7	0.89	3.00	0.39
430.9	0.59	0.92	0.16

Therefore, excitation at 430.7 nm and 215.35 nm produces large relative PLIF signals that are reasonably balanced and thus similar intensifier and imager settings can be used to acquire both signals simultaneously. Additionally, the greater uniformity of the NO + CH integrated signal as a function of wavelength and the near constant NO/CH ratio around 430.7 nm reduces sensitivity to small variations in the OPO signal wavelength. In general, a 430.9-nm excitation provides insufficient signal even though the NO and CH PLIF signals are well balanced. As a result, 430.7 nm was selected as the optimal OPO signal wavelength for the current work. The CH and NO PLIF images in Figs. 2(b) and 2(c) were acquired with an OPO signal of 430.7 nm and intensifier gains of 60% and 70%, respectively, and show sufficient signal levels, spatial resolution, and noise figures to enable semi-quantitative analysis of flame features. This is particularly important in turbulent diffusion flames where single-shot imaging is required, as will be discussed in Section 4.

For the specific system optimization in this work, corrections applied for calculation of absolute PLIF intensity were not required to enable the selection of the OPO signal and, therefore, the CH and NO PLIF excitation wavelengths. However, future work could extend this analysis to general systems by considering corrections for quenching, reabsorption of fluorescence, and differences in transmission of the filters and UV lens. Additionally, the wavelength selection in this work was optimized based on the NO concentrations present in NH₃-seeded flames. Combustion processes with lower levels of NO may benefit from an OPO signal wavelength of 429.8 nm, closer to the NO absorption peak.

4. DEMONSTRATION OF SINGLE-SHOT CH-NO PLIF AND RAYLEIGH SCATTERING IN A TURBULENT DIFFUSION FLAME

A. Flame Details and Image Quality

A series of single-shot NO and CH PLIF images were acquired in a CH₄-H₂-NH₃ diffusion flame with Reynolds Number of 7570 to demonstrate the utility of the diagnostic system for semiquantitative measurements of flame properties. A visual time-averaged image of the flame is shown in Fig. 3(a). The outer edge of the flame layer can be clearly identified and exhibits linear growth as a function of height above the surface, in line with self-similar solutions at stoichiometric conditions [35]. When fit with a linear function, the flame half width, $W_F(y)$, can be described as

$$W_F(y) = 0.114y + 1.01[\text{mm}],$$

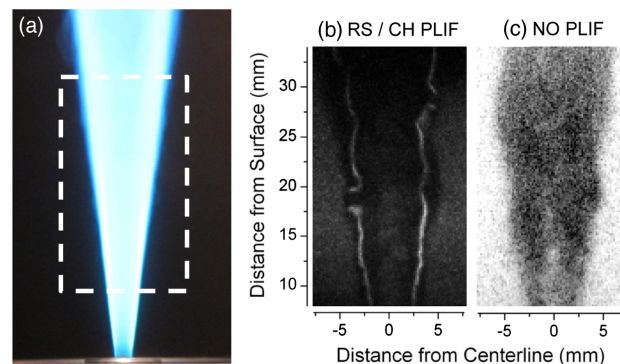


Fig. 3. (a) Visual image of the turbulent, non-premixed CH₄-H₂-NH₃ diffusion flame. The white box indicates the region of interrogation for (b) CH PLIF and (c) NO PLIF images. Color scaling is (b) reversed between images and (c) to enhance visual contrast. Rayleigh scattering from the ambient co-flow air and low-temperature fuel core is visible in the CH image.

where y is the height above the surface in mm. The flame has a half width of 1.01 mm at the burner surface, a half angle of 6.48°, and exhibits a virtual origin, a , equal to -8.88 mm. The burner orifice has a radius of 1 mm. The white dashed box in Fig. 3(a) represents the interrogation region for NO and CH PLIF.

Two representative, independently acquired PLIF images of CH and NO are shown in Figs. 3(b) and 3(c), respectively. Each image was acquired under identical conditions using the same laser system and camera/intensifier combination described in the previous sections. For CH PLIF, the GG400 filter was used to block signal from NO PLIF. In this case, the intensifier gain could not be increased beyond 65% because of the presence of elastic scattering in the images. Rayleigh scattering at 430.7 nm from the ambient air co-flow and low-temperature jet core are visible in the image. For NO PLIF, a UG11 spectral filter was used to block Rayleigh scattering at 430.7 nm and the CH PLIF signal. The image exposure times of 150 ns were used for both images, although intensifier gain was increased to 85% for the NO PLIF image. The intensifier level for NO PLIF was higher than that used in the laminar diffusion flame to compensate for the lower NO levels and transmission losses associated with the UG11 filter. Although the NO PLIF signal in the current work is sufficient for the use of high-speed intensified cameras for image collection, the NO concentration in the flame products can reach 2000 ppm in these flames [4]. Using the intensifier response and assuming constant excitation energy, the same relative intensified NO PLIF signal could be collected at 100% intensifier gain for an NO concentration of ~200 ppm. This is similar to NO concentrations measured for the combustion of fuels without NH₃ (100–1000 ppm) [1]. However, the image noise of the intensifier increases exponentially with intensifier gain thus potentially limiting its utility for PLIF imaging above ~90% gain and limiting detection levels to ~1000 ppm.

The peak PLIF signal to background noise ratio (SNR) was calculated for each image. The CH PLIF image exhibits an SNR of ~105 : 1 in the thin flame layers while the NO PLIF image has an SNR of ~33 : 1. This SNR is a useful indicator of the ability to identify flame layers from background in noisy

data. Clearly, this is applicable to the CH PLIF image, as is evident from the image itself, but the NO PLIF image would be better characterized by the peak PLIF signal to PLIF signal-to-noise ratio (PSNR), since the NO layers are broad. Within the broad NO PLIF region, the PSNR is $\sim 3:1$. This implies that although the NO PLIF layer is clearly distinguished from the background signal, variations in the NO concentration can only be identified within $\pm 33\%$. In contrast, the CH PSNR is $\sim 8:1$, in line with prior published values [14]. The noise features appear larger within the NO PLIF image and may originate from the increased intensifier gain used for the NO PLIF image acquisition.

B. Identification of General Flame Structure

Qualitatively, the CH PLIF signal originates from the thin flame region of the diffusion flame. The image quality is comparable to previously published CH PLIF images [13,14], and several breaks in the flame layer can be identified. The broad signal outside the flame layer is due primarily to Rayleigh scattering from room temperature air since the images have been corrected for background scattering. Additionally, the low-temperature core of the fuel jet can be seen in the middle of the flame. In contrast, the NO PLIF images exhibit broad, featureless layers, and the signal exists primarily in the high-temperature products of the diffusion flame. Although the images in Figs. 3(b) and 3(c) are not recorded simultaneously, the high-temperature products are observed in similar locations for both images, where the NO appears primarily inside the diffusion flame layer. Additionally, the NO PLIF image lacks a signal along the lower portion of the flame centerline, roughly corresponding with the location of the fuel jet observed in the CH PLIF image.

Quantitatively, analysis of the Rayleigh scattering at 430.7 nm, the CH PLIF signal, and the NO PLIF signal demonstrate the complementary nature of the two-color CH–NO PLIF technique and provide further support for identification of specific flame structures. Radial profiles of Rayleigh scattering and PLIF signals are shown for CH and NO in Fig. 4 at heights of (a) 10 mm, (b) 12.5 mm, (c) 15 mm, (d) 20 mm, (e) 25 mm, and (f) 30 mm above the burner surface. These profiles are taken from the images in Figs. 3(b) and 3(c) and were selected to highlight the various flame structures. Generally, the CH PLIF signal and Rayleigh scattering is normalized to unity at the radial extremes (± 7.5 mm), since the images are corrected for variations in the beam profile using the Rayleigh scattering from the ambient air co-flow. In this case, the laser beam propagates from positive to negative distances from centerline, consistent with the slight decrease in signal observed on the negative half of the abscissa. The NO PLIF signal is normalized to the maximum signal in the image. Near the burner surface, the CH layers are clearly defined with broad Rayleigh scattering regions both inside and outside of the flame layers, identified with a reduced signal resulting from higher temperatures. The NO PLIF signal mirrors the Rayleigh scatter signal, but is inverted, with a broad radial distribution and small depression along the centerline. As height above the burner surface is increased, the distance between the CH layers increases while the features associated with Rayleigh scattering are broadened. The NO PLIF signal also broadens and the depression observed at $y = 10$ mm is no

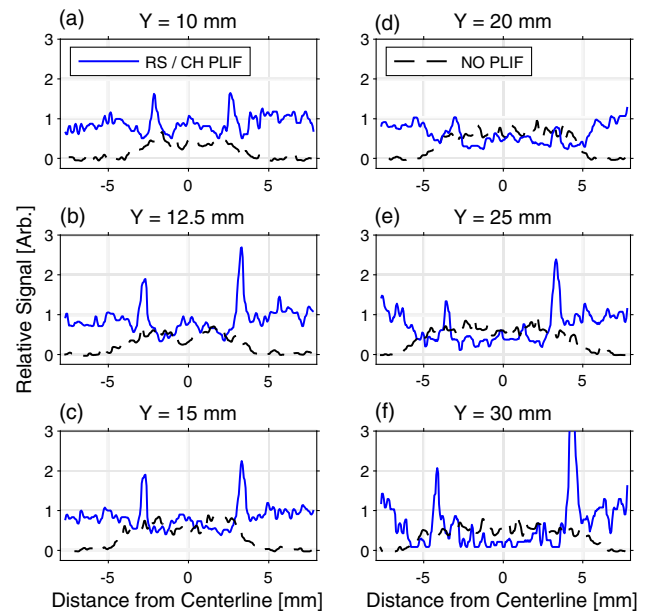


Fig. 4. CH PLIF and Rayleigh scatter at 430.7 nm (blue solid line) and NO PLIF (black dashed line) at heights of (a) 10 mm, (b) 12.5 mm, (c) 15 mm, (d) 20 mm, (e) 25 mm, and (f) 30 mm above the surface of the burner. The CH PLIF and Rayleigh scatter are normalized to Rayleigh scattering from the air co-flow. The NO PLIF is normalized to the peak signal in the image. Data are taken from single-shot images.

longer evident. Although the profiles in Fig. 4 are from a single set of images that were not acquired simultaneously and deviate from the average image as a result of the turbulent flame characteristics, the trends are consistent with all 200 images acquired in the data sets.

C. Quantification of Specific Flame Structure

Quantitative analysis of flame properties requires the identification of specific flame structures including flame layers, high-temperature products, and the fuel-jet core. The specific definition of these features enables measurement across sets of multiple images in a systematic way. Identification of these features is shown in Fig. 5(a) for Rayleigh scattering and CH PLIF and Fig. 5(b) for NO PLIF. The radial profiles shown were acquired at a height of 10 mm above the surface of the burner, for demonstration purposes. The high-temperature product region is identified by the region of the reduced Rayleigh scattering signal, RS_{Prod} , owing to the elevated temperature and lower density associated with those regions. The product region is fit with a super-Gaussian function. The low-temperature jet core of unburned fuel is identified by the increased Rayleigh scattering signal along the centerline, RS_{Core} , and is fit with a Gaussian function. Although the relative signal of the core is equal to that of the ambient air (~ 1), the Rayleigh scattering cross section of the fuel is $\sim 2\times$ that of air as a result of the high methane content (89.9% by volume). This indicates that the temperature of the core is ~ 600 K, which is reasonable assuming some mixing with products as evident in Fig. 3(c). The high-temperature CH layers are fit using Gaussian functions.

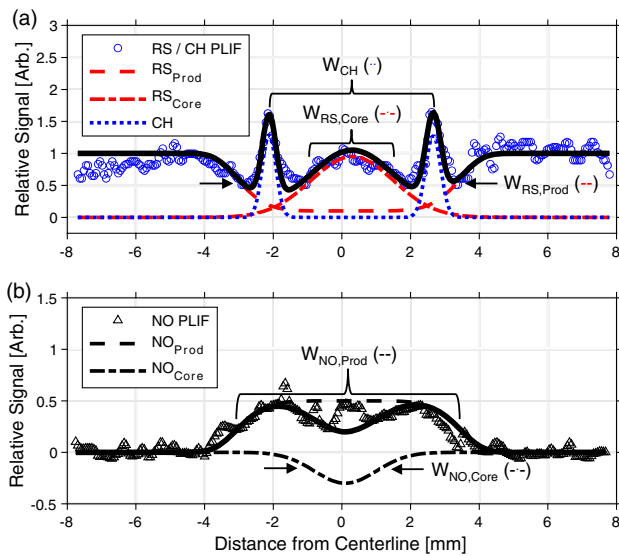


Fig. 5. (a) Identification of specific flame structures (combustion products, flame layers, fuel-jet core) originating from the CH PLIF and Rayleigh scatter and (b) from NO PLIF. Radial profiles were taken 10 mm above the burner surface from the CH and NO PLIF images in Figs. 3(b) and 3(c), respectively. Data are taken from single-shot images.

In Fig. 5(b), the high-temperature products region, NO_{Prod} , is identified with the NO PLIF signal and fit with a super Gaussian function. In this case, the order of the super Gaussian ($n = 3$) is identical to that used to fit RS_{Prod} . The low-temperature core, NO_{Core} , is associated with the depression in the NO signal along the centerline and fit with a Gaussian function. The total CH or NO PLIF signal can be reconstructed by taking the sum of the individual features, as shown in Figs. 5(a) and 5(b). This process was repeated on multiple image sets for radial profiles from 10–30 mm above the burner surface with steps of 2.5 mm. Using the fit parameters for the flame features shown in Figs. 5(a) and 5(b), quantitative values are calculated for the width of the flame layers, W_{CH} , the high-temperature product region, $W_{\text{RS,Prod}}$, and fuel core, $W_{\text{RS,Core}}$, based on Rayleigh scattering. The average measurements of the parameter half width at half maximum (HWHM) are given in Fig. 6(a) based on the CH PLIF image sets. For comparison, the average measurements of the high-temperature product, $W_{\text{NO,Prod}}$, and the fuel jet, $W_{\text{NO,Core}}$, HWHM are given in Fig. 6(b) based on the NO PLIF image sets. The dashed lines provide a reference to the burner orifice half width of 1 mm while the solid lines are the measured flame width from the visual image in Fig. 3(a). Several general trends are observed in the measured data.

First, the width of the fuel core is nearly equal to the orifice size. At 20 mm above the burner surface, the fuel-jet signal begins to dissipate. This reduction in radius most likely results from increased mixing between the fuel and burned products that dissipate and heat the jet, reducing the Rayleigh scattering signal. Increased mixing with the products is directly observed in the NO PLIF image where NO signal completely fills the interior of the diffusion flame above 20 mm. It is, therefore, not surprising that the fuel-jet half-width measurements from the

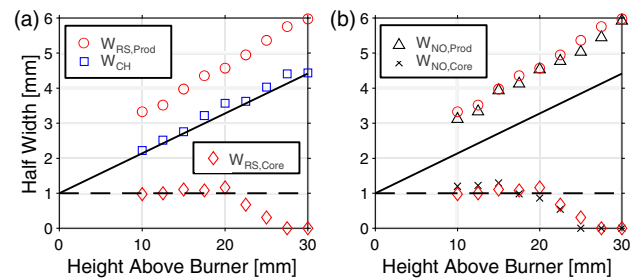


Fig. 6. Quantitative measurements of the combustion product zone half width, the flame layer half width, and fuel-jet half width from (a) CH PLIF and Rayleigh scattering and (b) NO PLIF. The dashed line indicates the burner orifice half width, and the solid line is the measured flame half width from Fig. 3(a).

Rayleigh scattering and NO PLIF signal are nearly identical, as shown in Fig. 6(b).

Second, the flame half width measured from the separation of the CH flame layers is a nearly linear function of the height above the burner and closely follows the flame width measured from the visual image as shown with a solid line. When fit with a linear function, the data yield a flame half width of 1.09 mm at the burner surface, a half angle of 6.66° , and a virtual origin of -9.31 mm. These metrics, computed from the CH PLIF and Rayleigh scatter images in Fig. 3(b), represent percent differences of 7.7%, 4.8%, and 2.7%, respectively, from the visual image measurements, and are indicative of the quantitative nature of the flame measurements derived from the current data sets.

Third, the region comprising the combustion products is observed to be broader than the flame width with a nearly constant offset of 1.14 ± 0.18 mm. This region exhibits a higher temperature than the surrounding co-flow of air as indicated by the reduction in Rayleigh scatter intensity. Although a full treatment of the Rayleigh scattering cross section of the products requires detailed knowledge of the chemical composition at each point in space and time, the product composition was computed using equilibrium chemistry, and the Rayleigh cross section was estimated to be $\sim 10\%$ higher than that of air [29]. If one assumes the products are well mixed 25 mm above the surface of the burner, a centerline temperature of 840 K is calculated from the Rayleigh scattering signal with uncertainty bounds of 650–1220 K based on the signal-to-noise ratio. The half width of the NO PLIF signal closely follows the Rayleigh scattering, as shown in Fig. 6(b), indicating this region is dominated by combustion products.

Quantitative comparisons of the CH and NO PLIF images yield information on the internal structure of turbulent diffusion flames, including the location of high-temperature flames and combustion products, and the persistence of the internal fuel core. Specifically, Rayleigh scattering at 430.7 nm and NO PLIF signals were used to identify combustion product zones and the low-temperature fuel core. Thus, the NO PLIF signal resulting from 215.35-nm excitation provides corroborating and complementary information to the Rayleigh scattering and CH PLIF signals originating from the 430.7-nm excitation.

5. SUMMARY AND EXTENSION TO KHZ-RATE DIAGNOSTICS

An optical parametric oscillator with second harmonic generation has been developed, which simultaneously produces sufficient laser light at 430.7 nm (2.5 mJ) and 215.35 nm (225 μ J) for CH–NO PLIF and Rayleigh scattering in laminar and turbulent diffusion flames with a mixture of fuels containing CH₄, H₂, and, NH₃. The CH A-X (0,0) and NO A-X (1,0) bands were chosen based on their accessibility, and appropriate spectral filters were applied to isolate NO PLIF, CH PLIF, and Rayleigh scattering at 430.7 nm. An optimal OPO signal wavelength was selected based on available pulse energies at UV and near-UV wavelengths, interferences from elastic scatter and broadband absorbers, and CH–NO PLIF intensity. Three potential wavelengths were identified, with selection of 430.7 nm, and 215.35 nm via SHG, based on three quantitative metrics relating the total signal level, the balance between CH and NO PLIF, and sensitivity to changes in the wavelength. The CH–NO PLIF and Rayleigh scattering approach and use of a high-speed, intensified imaging system was demonstrated in a turbulent, non-premixed diffusion flame. The image quality was quantified with sufficient SNR and spatial resolution to enable identification of general and specific flame structures. The quantitative measurements of the product region, flame layer, and fuel-jet half widths were achieved, demonstrating the complementary nature of the CH–NO PLIF and Rayleigh scattering approach.

Due to the limitations of using a single camera/intensifier system in the current work, single-shot pure CH and NO PLIF images were acquired independently. This prevented direct comparison of the pure signals outside the statistical averages, which were captured at different times in the turbulent diffusion flame. However, each single-shot image was acquired with appropriate spectral filters (GG400 or UG11) to suppress out-of-band signal. As such, simultaneous acquisition is straightforward using a second high-speed camera/intensifier system. In that case, one system could utilize a GG400 filter for capturing CH PLIF and Rayleigh scattering, while the second could utilize a UG11 filter for recording NO PLIF. Additionally, the high-speed pumping of the OPO described in this work has been demonstrated with sufficient signal for 10-kHz CH PLIF using a high-speed camera/intensifier system [13]. Therefore, extension of the current work to kHz rates is feasible with the addition of a second high-speed detection system.

Funding. National Science Foundation (Graduate Research Fellowship Program); Erlangen Graduate School of Advanced Optical Technologies.

Acknowledgment. The authors are grateful for insights from Drs. P. Kumar and M. Li, formerly of Iowa State University, regarding the combustion of fuels with NH₃. J. Miller was supported, in part, by the NSF Graduate Research Fellowship Program.

Disclosures. The authors declare no conflicts of interest.

REFERENCES

1. S. R. Turns, *An Introduction to Combustion: Concepts and Applications* (McGraw-Hill, 2011).
2. R. D. Stachler, J. S. Heyne, S. Stouffer, and J. D. Miller, "Lean blowoff in a toroidal jet-stirred reactor: Implications for alternative fuel approval and potential mechanisms for autoignition and extinction," *Energy Fuels* **34**, 6306–6316 (2020).
3. P. Kumar and T. R. Meyer, "Experimental and modeling study of chemical-kinetics mechanisms for H₂–NH₃–air mixtures in laminar premixed jet flames," *Fuel* **108**, 166–176 (2013).
4. M. Li, "A numerical and experimental study of in-situ NO formation in laminar NH₃-seeded syngas diffusion flames," Ph.D. thesis (Iowa State University, 2011).
5. S. V. Naik and N. M. Laurendeau, "Effects of CH–NO interactions on kinetics of prompt NO in high-pressure counterflow flames," *Energy Fuels* **22**, 250–261 (2007).
6. B. Thurow, N. Jiang, and W. R. Lempert, "Review of ultra-high repetition rate laser diagnostics for fluid dynamic measurements," *Meas. Sci. Technol.* **24**, 012002 (2013).
7. I. Boxx, M. Stohr, C. Carter, and W. Meier, "Temporally resolved planar measurements of transient phenomena in a partially pre-mixed swirl flame in a gas turbine model combustor," *Combust. Flame* **157**, 1510–1525 (2010).
8. S. Hammack, C. Carter, C. Wuensche, and T. Lee, "Continuous hydroxyl radical planar laser imaging at 50 kHz repetition rate," *Appl. Opt.* **53**, 5246–5251 (2014).
9. J. R. Osborne, S. A. Ramji, C. D. Carter, S. Peltier, S. Hammack, T. Lee, and A. M. Steinberg, "Simultaneous 10 kHz TPIV, OH PLIF, and CH₂O PLIF measurements of turbulent flame structure and dynamics," *Exp. Fluids* **57**, 65 (2016).
10. S. D. Hammack, C. D. Carter, A. W. Skiba, C. A. Fugger, J. J. Felver, J. D. Miller, J. R. Gord, and T. Lee, "20 kHz CH₂O and OH PLIF with stereo PIV," *Opt. Lett.* **43**, 1115–1118 (2018).
11. C. D. Carter, S. Hammack, and T. Lee, "High-speed planar laser-induced fluorescence of the CH radical using the C₂Σ⁺–X₂Π(0,0) band," *Appl. Phys. B* **116**, 515–519 (2014).
12. S. Hammack, J. R. Gord, C. D. Carter, and T. Lee, "Nitric oxide PLIF at 10 kHz in a seeded flow, a plasma discharge, and a flame," *Opt. Lett.* **51**, 8817–8824 (2012).
13. J. D. Miller, S. R. Engel, T. R. Meyer, T. Seeger, and A. Leipertz, "High-speed CH planar laser-induced fluorescence imaging using a multimode-pumped optical parametric oscillator," *Opt. Lett.* **36**, 3927–3929 (2011).
14. J. D. Miller, S. R. Engel, J. W. Troeger, T. R. Meyer, T. Seeger, and A. Leipertz, "Characterization of a CH planar laser-induced fluorescence imaging system using a kHz-rate multimode-pumped optical parametric oscillator," *Appl. Opt.* **51**, 2589–2600 (2012).
15. J. Sjöholm, E. Kristensson, M. Richter, M. Alden, G. Goritz, and K. Knebel, "Ultra-high-speed pumping of an optical parametric oscillator (OPO) for high-speed laser-induced fluorescence measurements," *Meas. Sci. Technol.* **20**, 025306 (2009).
16. N. B. Jiang, M. C. Webster, and W. R. Lempert, "Advances in generation of high-repetition-rate burst mode laser output," *Appl. Opt.* **48**, B23–B31 (2009).
17. M. N. Slipchenko, J. D. Miller, S. Roy, J. R. Gord, S. A. Danczyk, and T. R. Meyer, "Quasi-continuous burst-mode laser for high-speed planar imaging," *Opt. Lett.* **37**, 1346–1348 (2012).
18. M. N. Slipchenko, J. D. Miller, S. Roy, T. R. Meyer, J. G. Mance, and J. R. Gord, "100 kHz, 100 ms, 400 J burst-mode laser with dual-wavelength diode-pumped amplifiers," *Opt. Lett.* **39**, 4735–4738 (2014).
19. J. D. Miller, N. Jiang, M. N. Slipchenko, J. G. Mance, T. R. Meyer, S. Roy, and J. R. Gord, "Spatiotemporal analysis of turbulent jets enables by 100-kHz, 100-ms burst-mode particle image velocimetry," *Exp. Fluids* **57**, 192 (2016).
20. N. Jiang, M. Webster, W. R. Lempert, J. D. Miller, T. R. Meyer, C. B. Ivey, and P. M. Danehy, "MHz-rate nitric oxide planar laser-induced fluorescence imaging in a Mach 10 hypersonic wind tunnel," *Appl. Opt.* **50**, A20–A28 (2011).

21. J. D. Miller, M. Slipchenko, T. R. Meyer, N. B. Jiang, W. R. Lempert, and J. R. Gord, "Ultra-high-frame-rate OH fluorescence imaging in turbulent flames using a burst-mode optical parametric oscillator," *Opt. Lett.* **34**, 1309–1311 (2009).
22. N. Jiang, R. A. Patton, W. R. Lempert, and J. A. Sutton, "Development of high-repetition rate CH PLIF imaging in turbulent non-premixed flames," *Proc. Combust. Inst.* **33**, 767–774 (2011).
23. K. N. Gabet, R. A. Patton, N. Jiang, W. R. Lempert, and J. A. Sutton, "High-speed CH₂O PLIF imaging in turbulent non-premixed flames using a pulse burst laser system," *Appl. Phys. B* **106**, 569–575 (2012).
24. R. Pan, U. Retzer, T. Werblinski, M. N. Slipchenko, T. R. Meyer, L. Zigan, and S. Will, "Generation of high-energy, kilohertz-rate narrowband tunable ultraviolet pulses using a burst-mode dye laser system," *Opt. Lett.* **43**, 1191–1194 (2018).
25. I. Chtereov, N. Rock, H. Ek, B. Emerson, J. Seitzman, N. Jiang, S. Roy, T. Lee, J. R. Gord, and T. Liewen, "Simultaneous imaging of fuel, OH, and three component velocity fields in high pressure, liquid fueled, swirl stabilized flames at 5 kHz," *Combust. Flame* **186**, 150–165 (2017).
26. S. Roy, N. Jiang, P. S. Hsu, T. Yi, M. N. Slipchenko, J. J. Felver, J. Estevadeordal, and J. R. Gord, "Development of a three-legged, high-speed, burst-mode laser system for simultaneous measurements of velocity and scalars in reacting flows," *Opt. Lett.* **43**, 2704–2707 (2018).
27. J. A. Sutton and J. F. Driscoll, "Optimization of CH fluorescence in flames: Range of applicability and improvements with hydrogen addition," *Appl. Opt.* **42**, 2819–2828 (2003).
28. J. Luque and D. R. Crosley, "LIFBASE: Database and spectral simulation program (Version 1.5)," SRI International MP 99-009 (1999).
29. Z. S. Li, J. Kiefer, J. Zetterberg, M. Linvin, A. Leipertz, X. Bai, and M. Alden, "Development of improved PLIF CH detection using an Alexandrite laser for single-shot investigation of turbulent and lean flames," *Proc. Combust. Inst.* **31**, 727–735 (2007).
30. K. A. Watson, K. M. Lyons, C. D. Carter, and J. M. Donbar, "Simultaneous two-shot CH planar laser-induced fluorescence and particle image velocimetry measurements in a lifted CH₄/air diffusion flame," *Proc. Combust. Inst.* **29**, 1905–1912 (2002).
31. J. A. Sutton and J. F. Driscoll, "Rayleigh scattering cross sections of combustion species at 266, 355, and 532 nm for thermometry applications," *Opt. Lett.* **29**, 2620–2622 (2004).
32. R. A. Patton, K. N. Gabet, N. Jiang, W. R. Lempert, and J. A. Sutton, "Multi-kHz temperature imaging in turbulent non-premixed flames using planar Rayleigh scattering," *Appl. Phys. B* **108**, 377–392 (2012).
33. F. Z. Chen, D. L. Judge, C. Y. R. Wu, and J. Caldwell, "Low and room temperature photoabsorption cross sections of NH₃ in the UV region," *Planet. Space Sci.* **47**, 261–266 (1999).
34. J. Kiefer, F. Ossler, Z. S. Li, and M. Alden, "Spectral interferences from formaldehyde in CH PLIF flame front imaging with broadband B-X excitation," *Combust. Flame* **158**, 583–585 (2011).
35. Y. Kang, T. Lu, X. Lu, X. Gou, X. Huang, S. Peng, X. Ji, Y. Zhou, and Y. Song, "On predicting the length, width, and volume of the jet diffusion flame," *Appl. Therm. Eng.* **94**, 799–812 (2016).